Contents lists available at ScienceDirect

Transactions of Nonferrous Metals Society of China

36(2026) 818−829

www.tnmsc.cn

Mechanical properties and deformation mechanisms of Ni−Co-based wrought superalloy via solution−rolling−aging treatment

Yao ZHANG [a], Jin-lin LI [a], Yan-cheng LI [a], Jin-xin DONG [b,c], Cai-yu GUO [b,d], Hong-yao YU [b,d,**], Qing WANG [a,*]

[a] School of Materials Science and Engineering, Dalian University of Technology, Dalian 116024, China;

[b] Beijing Key Laboratory of Advanced High Temperature Materials, Central Iron & Steel Research Institute, Beijing 100081, China;

[c] School of Materials Science and Engineering, Lanzhou University of Technology, Lanzhou 730050, China;

[d] Gaona Aero Material Co., Ltd., Beijing 100081, China

Abstract: To achieve high strength in Ni−Co-based wrought superalloys, cold-rolling was introduced into the solution and aging treatments. The alloys were characterized and tested using EBSD, SEM, TEM, and tensile tester to analyze their microstructure and mechanical properties at different temperatures, revealing their strengthening and deformation mechanisms. Results indicated that after solution, cold-rolling, and double aging, the alloy contained high-density dislocations, stacking faults, Lomer−Cottrell locks, and nanotwins. The yield strengths of the alloy at room temperature, 923, and 1023 K were 1855, 1406, and 1086 MPa, respectively, which were significantly higher than those of typical Ni-based wrought superalloys. This enhancement was primarily attributed to the dislocations and nanotwins. Additionally, during the cold-rolling process, plastic deformation mainly occurred through dislocation slip. With the temperature increasing to 923 and 1023 K, the main deformation mechanisms of the alloy transformed to stacking faults and nanotwins, respectively.

Keywords: Ni−Co-based wrought superalloy; mechanical properties; dislocations; stacking faults; nanotwins

1 Introduction

Ni-based wrought superalloys have been widely used as fasteners, blades, and discs for advanced aircraft engines due to their excellent mechanical properties at high-temperatures (HTs), such as high strength and creep rupture lifetime [1−3]. These superalloys are usually strengthened by γ'-Ni_3Al ($L1_2$-Cu_3Au type) or γ''-Ni_3Nb (tetragonal $D0_{22}$-Al_3Ti type) [4]. By contrast, the γ/γ' coherent microstructure is more stable at HTs because the $L1_2$-γ' phase is the ordered super-structure of FCC-γ solid solution [5]. Thus, the IN 718 Plus alloy (Ni−9Co−9.2Fe−19Cr−2.8Mo−1.08W−1.58Al−0.8Ti−5.5Nb−0.04C−0.005B, in wt.%, hereafter the same) exhibits a higher strength (σ_{YS}=940 MPa at 973 K) than IN 718 (Ni−19Fe−19Cr−3.1Mo−0.55Al−0.95Ti−5.3Nb−0.03C−0.005B) alloy (σ_{YS}=760 MPa at 973 K), which is ascribed to the strengthening of γ' nanoprecipitates with a volume fraction of about 25% [1,4]. In order to further enhance the HT strength, the U720 (Ni−14.8Co−18.0Cr−3.0Mo−1.5W−2.4Al−4.8Ti−0.05C−0.040B−0.03Zr) [6], U720Li (Ni−14.4Co−15.9Cr−3.0Mo−1.3W−2.5Al−5.0Ti−0.014C−0.014B) [7], and TMW-4M3 (Ni−25Co−13.5Cr−2.8Mo−1.2W−2.3Al−6.2Ti−0.03C−0.02B−0.03Zr) alloys have been developed by increasing the amount of γ'-forming elements [8], in which the volume fraction of γ' nanoprecipitates exceeds 40%. Especially,

Corresponding author: *Qing WANG, Tel: +86-13998523914, E-mail: wangq@dlut.edu.cn;
**Hong-yao YU, Tel: +86-17744595852, E-mail: hongyao21@163.com

https://doi.org/10.1016/S1003-6326(25)66999-8
Received 30 June 2024; accepted 21 January 2025

the TMW-4M3 superalloy demonstrates an impressive yield strength of 1008 MPa at 1023 K and shows exceptional creep resistance, with a lifetime exceeding 850 h when subjected to conditions of 998 K and 480 MPa [9]. Although the HT mechanical properties and thermal stability of γ/γ' coherent microstructure have been further enhanced by composition optimization, the solvus temperature and volume fraction of γ' phase increase, which significantly degrades the processibility of superalloys [10].

Recently, the prefabrication and tailoring of substructures (such as nanotwins) in alloys have been widely applied to improving both strength and ductility [11]. For instance, the introduction of high-density nanotwins into Ni-based superalloy can increase the yield strength from 1030 to 1235 MPa at room temperature (RT) and from 924 to 1077 MPa at 1033 K, respectively [12]. In fact, the formation of nanotwins is strongly dependent on the stacking fault energy (SFE), which is related to the alloy composition [13]. It has been demonstrated that the addition of Co can decrease the SFE of the TMW series alloys, in which the lowest SFE appears in the superalloy containing 25 wt.% Co [14]. Additionally, the deformation conditions can also affect the formation of SFs and nanotwins [15], as evidenced by the fact that the deformation mechanism of TMW-4M3 alloy with low SFE ((19.9±2.5) mJ/m^2) at RT is dominated by dislocation pairs shearing precipitates, while the deformation mechanisms at 923 and 998 K are controlled by SFs and nanotwins shearing precipitates, respectively. By contrast, only the Orowan looping process combining dislocation slip and climb occurs in the U720Li alloy with a higher SFE ((35.9±3.7) mJ/m^2) during the tensile deformation from RT to 998 K, resulting in lower strength at 923−1023 K [16].

In previous works, most research focused mainly on the change of chemical composition and heat-treated processing to modulate the γ' particles (particle size, morphology, and volume fraction) for achieving high strength of Ni-based wrought superalloys. However, the introduction of cold working during complex heat treatments to improve the mechanical properties of superalloys has rarely been investigated. In the present work, we introduced substructures by cold-rolling process to improve the strength of a novel Ni−Co-based wrought superalloy. The alloy has a composition of Ni−24.96Co−13.12Cr−2.80Mo−1.16W−2.51Al−4.43(Ti+Nb)−0.07(C+B+Zr). A complete processing sequence, including solid-solution treatment, cold-rolling, and double-aging, was executed. The microstructure of the treated superalloy was firstly characterized, followed by measurements of its tensile properties at RT and HTs (923 and 1023 K), along with a detailed discussion of the strengthening mechanisms at RT. Combined with the microstructural characterization of the deformed alloy, the deformation mechanisms at HTs were also explored. These results will be essential for understanding the effects of cold-rolling and optimizing the properties of Ni−Co-based superalloys.

2 Experimental

The material used in the present investigation was prepared via vacuum induction melting (VIM), electroslag remelting (ESR), and vacuum consumable remelting (VAR). After the high-temperature homogenization treatment, the superalloy ingot was forged into disc measuring d500 mm × 65 mm. Experimental samples were taken in tangential direction from the center to 1/2 of the disk rim. The hot-forged alloy samples were subjected to solution treatment at 1323 K for 4 h, cold-rolling with a deformation of 40%, and double-aging at 923 K for 24 h and then at 1033 K for 16 h. After each heat treatment, the samples were cooled to room temperature in air.

The (111) diffraction peak was precisely scanned at a rate of 1 (°)/min using a Bruker D8 X-ray diffractometer with Cu K_α radiation (XRD, λ=0.15406 nm). The resulting peak was then fitted with the pseudo-Voigt function in Origin software to calculate the lattice constants of γ and γ' phases [17]. The microstructure characterization was carried out using an IT800−SHL field emission scanning electron microscope (FE-SEM) equipped with an electron backscatter diffraction (EBSD) system. For SEM analysis, the etching solution comprised 42 mL H_3PO_4, 34 mL H_2SO_4, and 24 mL H_2O. For EBSD analysis, the electro-polishing solution comprised 10 mL $HClO_4$ and 90 mL C_2H_5OH. The EBSD acceleration voltage was set as 20 kV, the step size was 0.3, and the sample inclination angle was 70°. More detailed microstructure characterization was carried out with a JEM2100FFEG transmission electron microscope

(TEM). TEM specimens were firstly punched into circular sheets with a diameter of 3 mm and then ground to approximately 50 μm. They were subsequently subjected to twin-jet electron-polishing using the mixed solution of 5 mL $HClO_4$ and 95 mL CH_3OH at a temperature around 243 K. Using ImageJ software, a large number of precipitates for the aged state were hand-traced across more than 6 SEM morphology images. The average radius (r) of precipitates was calculated via a circular-equivalent [18]. Additionally, the volume fraction (f) of precipitates was determined based on the area fraction. Uniaxial tensile tests at RT, 923 K, and 1023 K were carried out on a UTM 5504 Material Test System (MTS) with a nominal strain rate of 3×10^{-4} s^{-1}. Three tensile samples with a gauge diameter of 5 mm and a length of 30 mm for each state were tested.

3 Results

3.1 Microstructure characteristics

Figure 1(a) shows the microstructure of the current Ni−Co-based wrought superalloy in the aged state, which clearly indicates that the alloy consists of elongated grains along the rolling direction with a size of (16±5) μm. In addition, it can be clearly observed from the corresponding kernel average misorientation (KAM) map that a large number of dislocations still exist in the aged alloy, as shown in Fig. 1(b). The SEM observations presented in Figs. 1(c, d) reveal that the current alloy displays a classical multi-size distribution of γ' precipitates. This includes coarse primary γ' precipitates located at grain boundaries (GBs), fine secondary γ' precipitates within the FCC-matrix, and ultrafine tertiary γ' nanoprecipitates surrounding the primary γ' particles. The particle size and volume fraction of three types of γ' particles were measured, being r_p=(378±112) nm and f_p=(11.6±2.3)%, r_s=(26±5) nm and f_s=(29.8±3.1)%, as well as r_t=(5±2) nm and f_t≈1%, respectively.

The aged alloy was further analyzed by the TEM to characterize the substructures, from which it could be found that a large number of dislocations prefabricated by cold-rolling were preserved in the FCC-γ matrix after aging, as presented in Figs. 2(a, b). Moreover, the tangled dislocations and

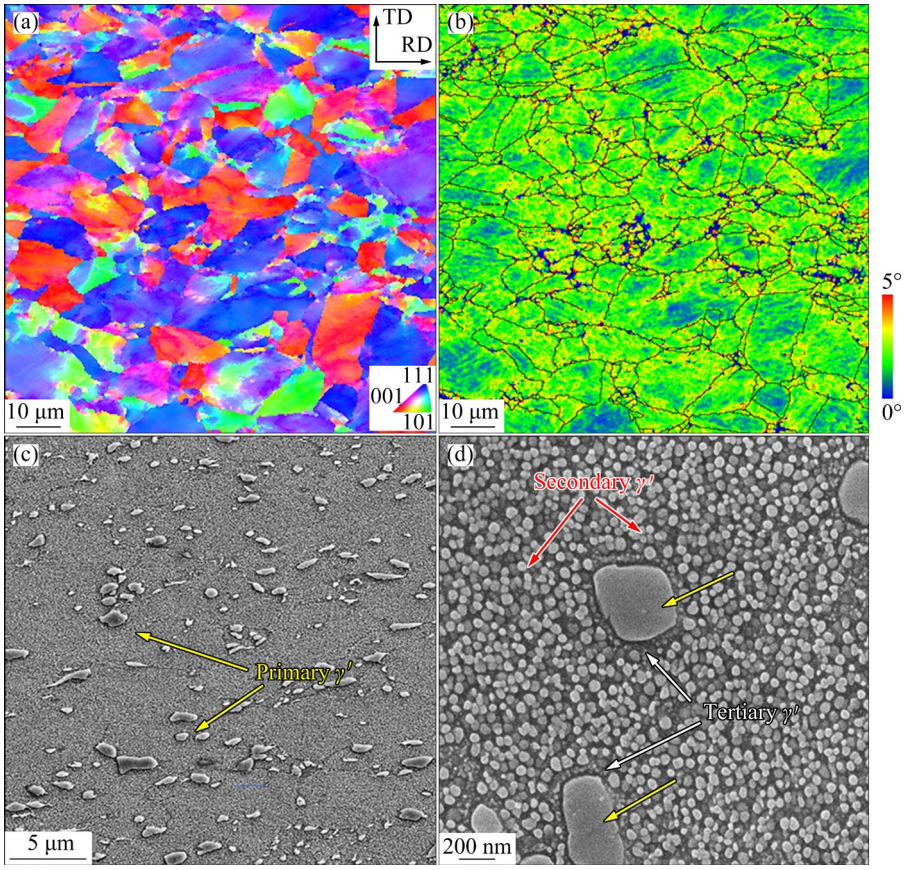

Fig. 1 Microstructural characterization results of aged superalloy: (a) Inverse pole figure (IPF); (b): KAM map; (c, d) SEM images

anti-phase boundaries (APBs) were also found in the coarse primary γ' particles (Fig. 2(a)). In addition, the SFs with a length of ~45 nm occurred in the γ matrix and some secondary γ' particles, in which the SFs with different orientations could be intersected at 71° to form Lomer−Cottrell (L−C) locks (Figs. 2(c, d)). Besides, nanotwins with a thickness of ~40 nm were also observed, as evidenced by the selected-area electron diffraction (SAED) patterns along the [110] direction (Figs. 2(e, f)).

3.2 Mechanical properties

Uniaxial tensile tests of the current superalloy were carried out at RT, 923 K, and 1023 K, and the engineering stress−strain curves are shown in Fig. 3. It can be seen that this superalloy has prominent mechanical properties, as exhibited by a high yield strength of σ_{YS}=1855 MPa and an ultimate tensile strength of σ_{UTS}=1986 MPa at RT. Although the strength decreases with increasing temperature, it still maintains a high level at HTs, being σ_{YS}=1406 MPa

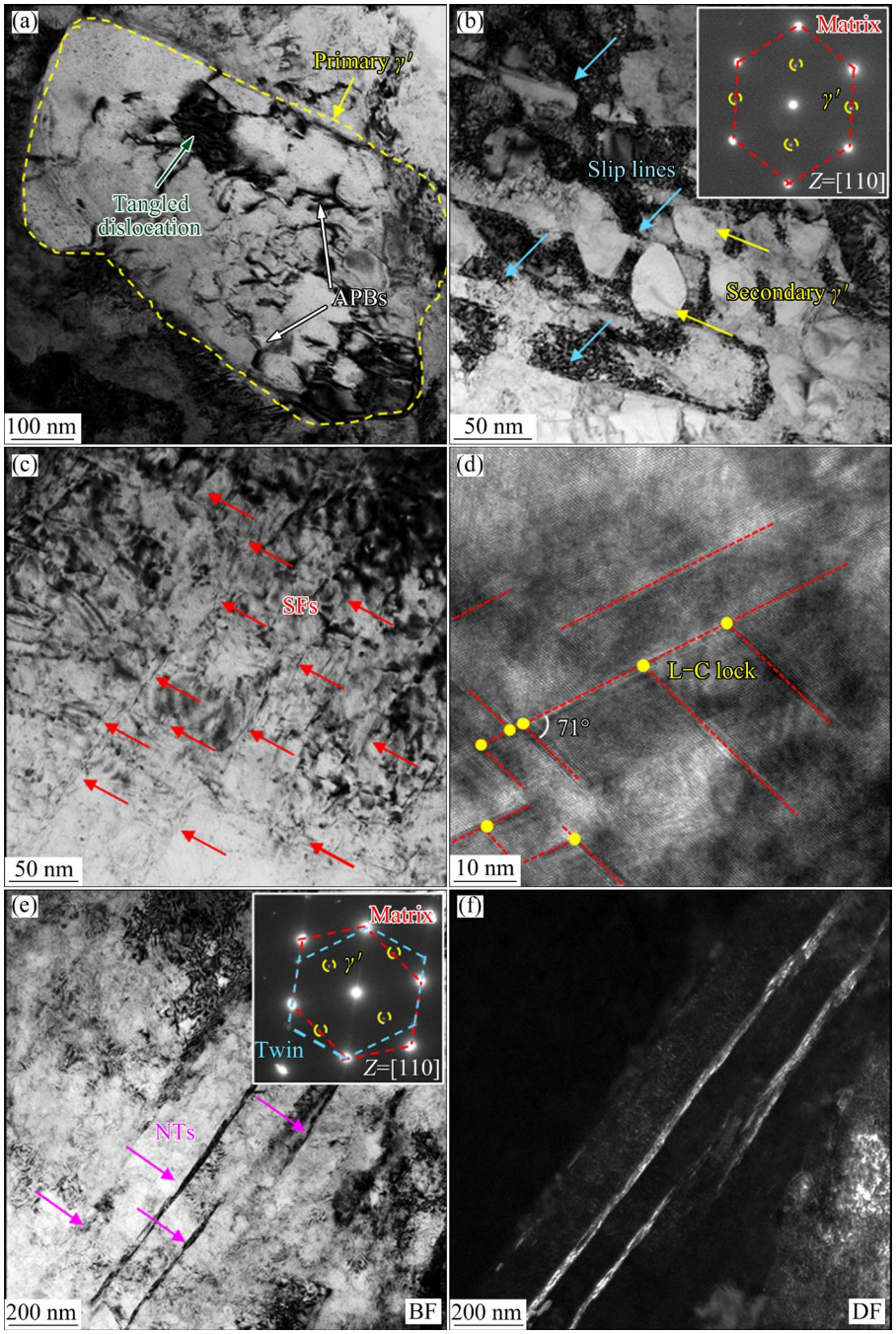

Fig. 2 TEM images of substructures in aged superalloy: (a−c) Bright-filed (BF) images showing tangled dislocations, APBs, slip lines, and SFs, respectively; (d) High-resolution TEM (HRTEM) image showing L−C locks; (e, f) BF and dark-field (DF) images showing nanotwins, respectively

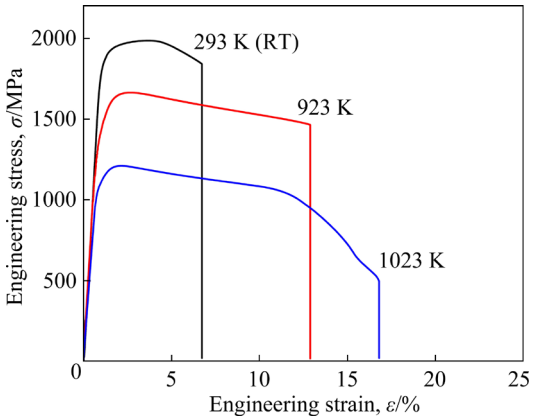

Fig. 3 Engineering stress−strain of current superalloy curves measured at RT, 923 K and 1023 K (Data from our previous work [19], re-plotted for the present study)

and σ_{UTS}=1663 MPa at 923 K, σ_{YS}=1086 MPa and σ_{UTS}=1208 MPa at 1023 K, respectively. Moreover, the elongation increases gradually from 7.6% to 13.0%, and then to 17.3% as the temperature changes from RT to 923 K, and then to 1023 K, respectively.

3.3 Microstructures after tensile tests

Figure 4 shows the TEM images of the alloy after tensile tests at 923 K, from which it can be seen that a large number of dislocations and SFs exist in the γ matrix, similar to those in the aged state. But differently, SFs were also observed in the primary γ' particles, besides the tangled dislocations and APBs, and the secondary γ' nanoparticles were severely deformed with abundant SFs with an average length of ~50 nm (Figs. 4(a, b)). Thus, the deformation of the alloy at 923 K was mainly dominated by shearing mechanism of SFs. The inverse fast Fourier transform (IFFT) image in Fig. 4(c) shows an enlarged view of the superlattice intrinsic stacking faults (SISFs) formed by the misalignment of ABCABCBCAB atoms. In addition, the number of nanotwins crossing the γ matrix and γ' nanoprecipitates increases while the thickness decreases to ~30 nm (Figs. 4(d, e)). The interactions among dislocations, SFs, and nanotwins in the deformed sample are more complex, as shown in Fig. 4(f).

Figure 5 exhibits the TEM images of the alloy after tensile test at 1023 K, from which it can be seen that the deformation mechanism was dominated by nanotwins. A large number of nanotwins crossing the γ matrix and γ' nanoparticles (primary and secondary) were observed in the alloy, as seen in the BF and DF images, as well as the inserted SAED patterns (Figs. 5(a−d)). Compared to the substructures in the 923 K-deformed sample, the amount of L−C locks and nanotwins was further increased, and a large number of multilayered nanotwins appeared, as presented in Fig. 5(e). In addition, SFs and SFs, nanotwins and nanotwins, and SFs and nanotwins were all intersected at 71°, indicating a more complex interaction among these substructures (Fig. 5(f)).

4 Discussion

4.1 Strengthening mechanism in Ni−Co-based wrought superalloy

The yield strength of the novel Ni−Co-based wrought superalloy subjected to solid-solution, cold-rolling, and double-aging in this study exhibited a significant enhancement at both RT and HTs. Specifically, we analyzed the contributions to the RT yield strength in light of the strengthening mechanisms, which came mainly from the lattice friction stress of pure Ni ($\Delta\sigma_0$=22 MPa) [20], atoms in solid-solution ($\Delta\sigma_S$), grain boundary ($\Delta\sigma_G$), and three types of γ' precipitates ($\Delta\sigma_P$), dislocation ($\Delta\sigma_D$) and nanotwin ($\Delta\sigma_T$). Therefore, the theoretical yield strength ($\Delta\sigma_{YS}$) of the alloy could be obtained from Eq. (1):

$$\Delta\sigma_{YS}=\Delta\sigma_0+\Delta\sigma_S+\Delta\sigma_G+\Delta\sigma_P+\Delta\sigma_D+\Delta\sigma_T \quad (1)$$

For the solid-solution strengthening, the contributions of the alloying elements in FCC-γ matrix are accounted with Eq. (2) [21]:

$$\Delta\sigma_S=(1-f_{\gamma'})[\sum_i (S_i^{\gamma})^2]^{1/2} \quad (2a)$$

$$S_i^{\gamma}=\beta_i^{\gamma}(X_i^{\gamma})^{1/2} \quad (2b)$$

where $f_{\gamma'}$ is the volume fraction of γ' phase; β_i^{γ} represents the solid-solution strengthening coefficient, reflecting the strengthening effects of solid-solution elements; X_i^{γ} denotes the content of element i in FCC matrix. The specific values of β_i^{γ} for Al, Ti, Nb, Cr, Mo, W, and Co in this current alloy are typically reported as 22.5, 77.5, 118.3, 33.7, 101.5, 235.9, and 39.4 MPa·at.%$^{-1/2}$, respectively [21]. Consequently, the enhancement in strength due to solid-solution strengthening of the alloy is $\Delta\sigma_S$=210 MPa.

The enhancement in strength resulting from grain boundary could be described using the Hall−Petch relationship, as shown in Eq. (3) [22,23]:

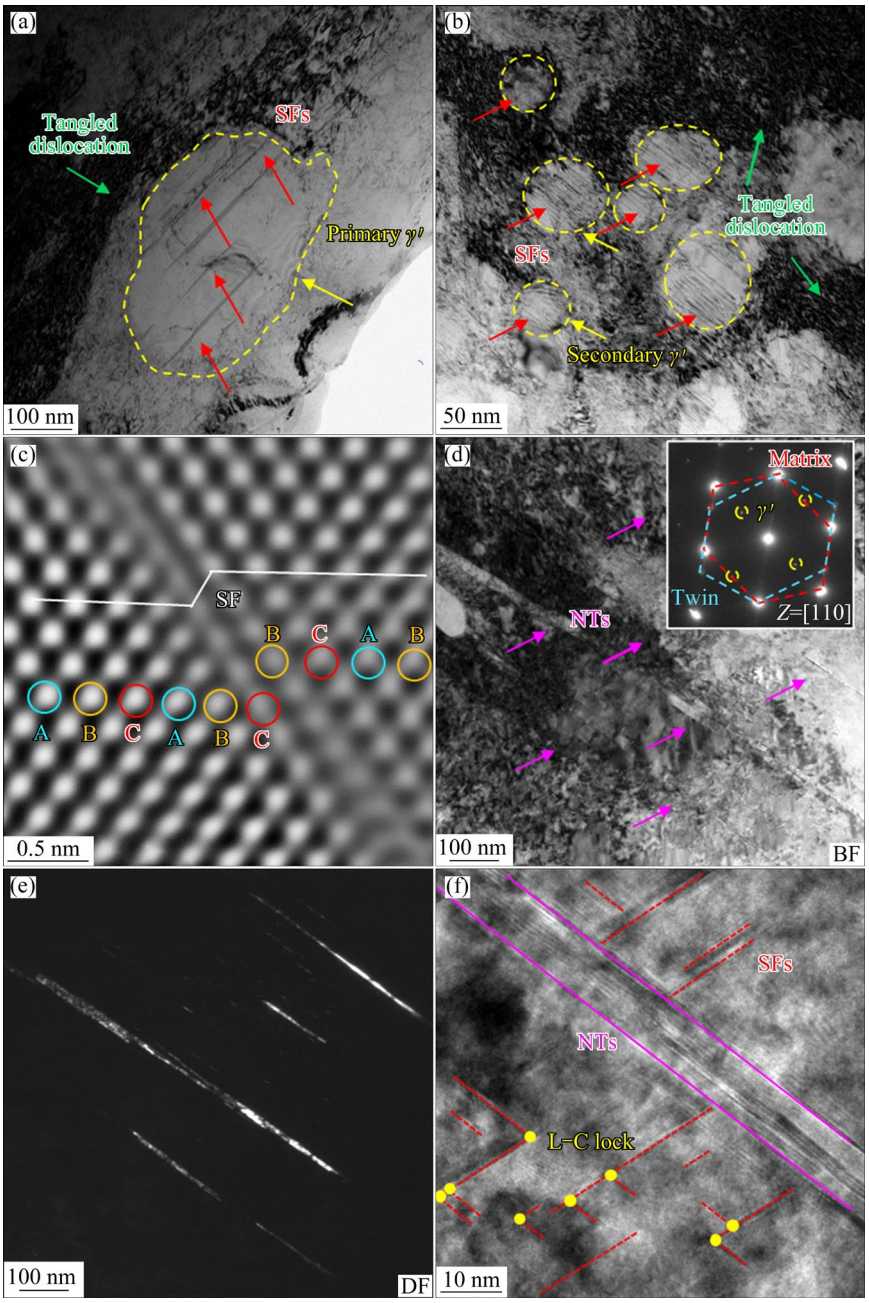

Fig. 4 TEM images of substructures in alloy deformed at 923 K: (a, b) BF images showing SFs in primary and secondary γ' nanoparticles; (c) IFFT image showing atomic structure of SISFs; (d, e) BF and DF images showing nanotwins, respectively; (f) HRTEM image showing interactions among nanotwins and SFs

$$\Delta\sigma_G=Kd^{-1/2} \quad (3)$$

where K and d are Hall−Petch coefficient and average grain size, respectively. For this current Ni−Co-based superalloy, the above parameters are K=750 MPa·μm$^{1/2}$ [21] and d≈16 μm. Therefore, the strength contribution from grain boundary in the current alloy is $\Delta\sigma_G$=188 MPa.

The precipitation strengthening could be categorized into two mechanisms: the Orowan mechanism and the shearing mechanism, which depend on how moving dislocations interact with precipitates [24,25]. The Orowan mechanism ($\Delta\sigma_{Orowan}$) dominates when the particles are large or incoherent with the matrix. In contrast, when nanoprecipitates are tiny and coherent with the matrix, particle shearing mechanism becomes effective. It contributes through both coherency strengthening ($\Delta\sigma_{CS}$) and modulus mismatch strengthening ($\Delta\sigma_{MS}$). The contribution from order strengthening ($\Delta\sigma_{OS}$) is considered negligible as

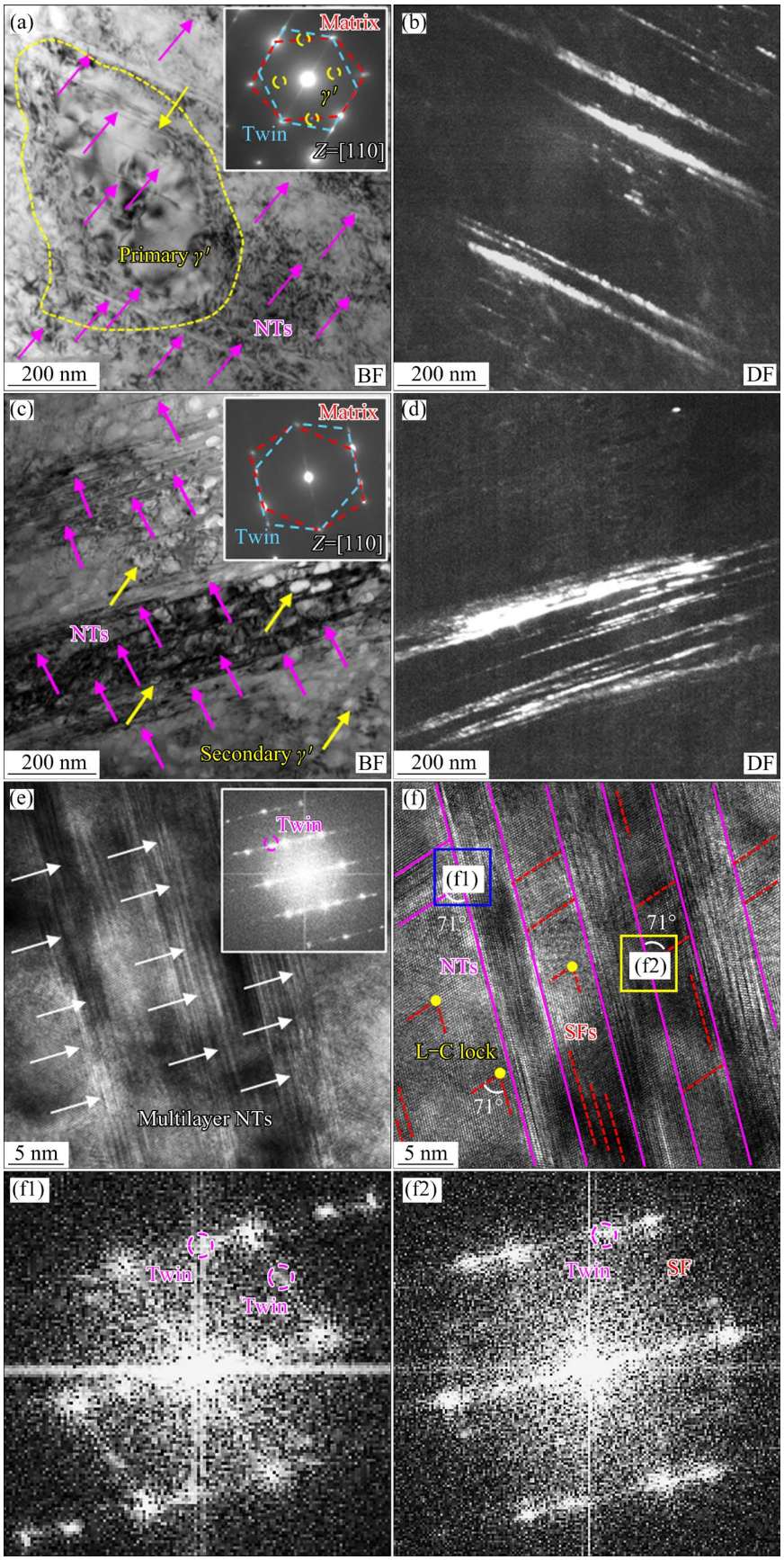

Fig. 5 TEM images of substructures in deformed alloy at 1023 K: (a−d) BF and DF images showing nanotwins across γ matrix and γ' nanoparticles; (e) HRTEM image showing multilayer nanotwins; (f) HRTEM image showing more complex interaction among substructures; (f1, f2) Corresponding FFT patterns of Regions f1 and f2, respectively

$L1_2$-γ' precipitates exhibit a low APB energy [26]. In fact, the Orowan bypassing and shearing mechanisms operate independently at the same time, while the contribution of the overall strengthening is governed by the minimum of ($\Delta\sigma_{CS}$+$\Delta\sigma_{MS}$) or $\Delta\sigma_{Orowan}$ [27]. The formulas used to obtain the strength enhancements are given by Eq. (4) [27,28]:

$$\Delta\sigma_{CS}=M\alpha_{\varepsilon}(G\delta_c)^{3/2}[rf_{\gamma'}/(0.5Gb)]^{1/2} \quad (4a)$$

$$\Delta\sigma_{MS}=0.0055M(\Delta G)^{3/2}(2f_{\gamma'}/G)^{1/2}(r/b)^{\frac{3m}{2}-1} \quad (4b)$$

$$\Delta\sigma_{Orowan}=M[0.4Gb/(\pi\sqrt{1-v})][\ln(2\sqrt{2/3}r/b)/\lambda_p] \quad (4c)$$

$$\lambda_p=2\sqrt{2/3}r\left[\sqrt{\pi/(4f_{\gamma'})}-1\right] \quad (4d)$$

where M, α_{ε}, m, δ_c, G, ΔG, b, v, and λ_p are Taylor factor, constant, constant, constrained lattice misfit, shear modulus for FCC-γ, shear modulus difference between FCC-γ and $L1_2$-γ', magnitude of Burgers vector, Poisson's ratio, and inter-precipitate distance, respectively. For the current Ni−Co-based superalloy, the above parameters are M=3.06 [29], α_{ε}=2.6, m=0.85 [30,31], G=81 GPa, ΔG=4 GPa [30,32], b=0.253 nm, v=0.35 [30,33], and λ_p can be obtained from the particle radius. The δ_c was calculated as δ_c=2ε/3=0.24% [34], where ε=0.36% is the lattice misfit obtained from Fig. S1 (Supplementary Materials). The current alloy exhibits three distinct sizes of γ' particles: the coarse primary precipitates alongside secondary and tertiary particles, which provide precipitation strengthening in significantly different ways. Due to their coarse size, primary γ' particles predominantly activate the Orowan mechanism, whereas the shearing mechanism becomes operative owing to the nano-scale dimensions of secondary and tertiary γ' particles, as shown in Fig. 6(a). Thus, the overall contribution of the precipitation strengthening is the sum of strength enhancement of the primary, secondary and tertiary γ' particles. This results in $\Delta\sigma_P$=$(\Delta\sigma_{Orowan})_p$ + ($\Delta\sigma_{CS}$+$\Delta\sigma_{MS}$)$_s$ + ($\Delta\sigma_{CS}$+$\Delta\sigma_{MS}$)$_t$ = 81 MPa + 635 MPa + 52 MPa = 768 MPa. Notably, the primary source of enhancement stems from secondary γ' nano-precipitates, being ($\Delta\sigma_{CS}$+$\Delta\sigma_{MS}$)$_s$= 635 MPa.

The current alloy has a high density of dislocations after cold-rolling and aging, leading to an increase in strength. The dislocation strengthening can be calculated according to Taylor's hardening law [35,36]:

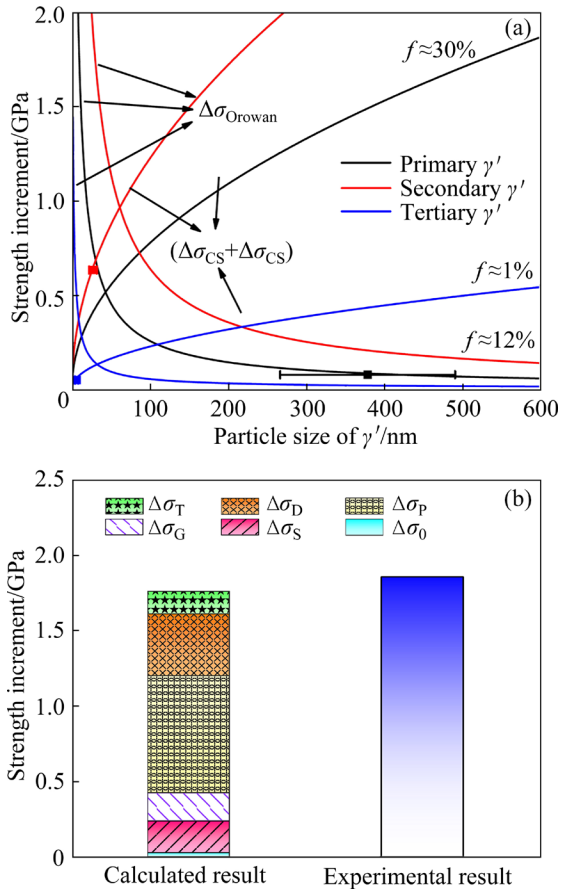

Fig. 6 (a) Calculation results of precipitation strengthening of three kinds of γ' particles; (b) Comparison of calculated and experimental values of yield strength at RT

$$\Delta\sigma_D=M\alpha Gb\rho^{1/2} \quad (5)$$

where ρ is the dislocation density. For the current Ni−Co-based superalloy, the above parameters are α=0.2 [37], and ρ=9.5×10^{14} m^{-2} calculated by EBSD (as seen in Fig. 1(b)). Consequently, the contribution of $\Delta\sigma_D$ is 387 MPa, which plays a key role in the increment of the yield strength of this alloy.

Twin boundary is a special kind of grain boundary. It can effectively impede dislocation motion and thus increase the yield strength of alloys [13,14,16]. In this study, a large number of nanotwins were prefabricated by cold-rolling, and thus the contribution of nanotwins to the yield strength is not negligible. The increment in yield strength from nanotwin boundaries can be described by Eq. (6) [38]:

$$\Delta\sigma_T=KV_Tt^{-1/2} \quad (6)$$

where V_T and t are volume fraction of nanotwins and average thickness of nanotwins, respectively. For

the current Ni−Co-based superalloy, the above parameters V_T≈4% and t≈40 nm (Figs. 2(e, f)). Consequently, the enhancement of nanotwins to yield strength in the current alloy is $\Delta\sigma_T$=150 MPa.

Finally, Fig. 6(b) presents a summary of the total contributions from each individual strength mechanism in the current alloy. The theoretical yield strength for the current alloy is calculated as $\Delta\sigma_{YS}=\Delta\sigma_0+\Delta\sigma_S+\Delta\sigma_G+\Delta\sigma_P+\Delta\sigma_D+\Delta\sigma_T$, which equals 1725 MPa. It is clear that the theoretical result is in reasonable agreement with the experimental result.

Moreover, the yield strength values of the alloy deformed at 923 and 1023 K are still high, being 1406 and 1086 MPa respectively, which are significantly higher than those of typically existing superalloys, indicating that the substructures of high-density dislocations, SFs, and nanotwins prefabricated by cold-rolling can play a crucial role in the enhancement of yield strength at elevated temperatures. Thus, treatment processes such as solid-solution treatment, cold-rolling, and double-aging can serve as effective means to improve the HT mechanical properties of Ni−Co-based wrought superalloys.

4.2 Deformation mechanisms in Ni−Co-based wrought superalloy

At low and intermediate temperatures (298−1073 K), dislocations interact with the γ' particles in two main ways, i.e., a pair of $a/2\langle110\rangle$ dislocations shear the γ' nanoparticles to form APBs or dissociate into partial dislocations to form SFs. These two modes are competitive, with the former prevailing in superalloys at temperatures below 873 K, whereas the latter is usually observed at higher temperatures [8,16]. It is shown that both the volume fraction of the γ' phase and temperature determine the dominance of the two mechanisms by affecting the relative magnitudes of the APB energy and the SF energy [14]. In the temperature range below 1023 K, the APB energy of the γ' phase changes slightly with increasing temperature, while the SF energy decreases significantly with increasing temperature [39]. In this study, temperature is the main factor affecting the two mechanisms since the tensile testing at different temperatures has little effect on the volume fraction of γ' particles. A large number of slip bands after the cold-rolling and double-aging treatment appear in the current alloy, indicating that plastic deformation in cold-rolling state is dominated by plane slip of dislocations in the γ matrix. This is mainly ascribed to the addition of Ti and Nb elements that increase the APB energy and create a stronger barrier to the dislocation shearing the γ' particle. In fact, SFs and nanotwins were also observed in the aged alloy (Fig. 2), which suggested that the SF and nanotwin shearing mechanisms also occurred during the cold-rolling. Moreover, dislocation reactions can occur during the deformation, as shown in Fig. 7(a). This often results in two partial dislocations interacting to form a L−C lock. In order to further view this reaction between dislocations, an IFFT image of the L−C lock is shown in Fig. 7(b), featuring a Burgers vector of $a/6[011]$. It is shown that the L−C lock is formed by the interaction of two partial dislocations, which are produced by the $a/2[110]$ and $a/2[\bar{1}10]$ full dislocations on $(\bar{1}11)$ and (111) slip planes, respectively. The specific reaction processes can be represented by Eq. (7):

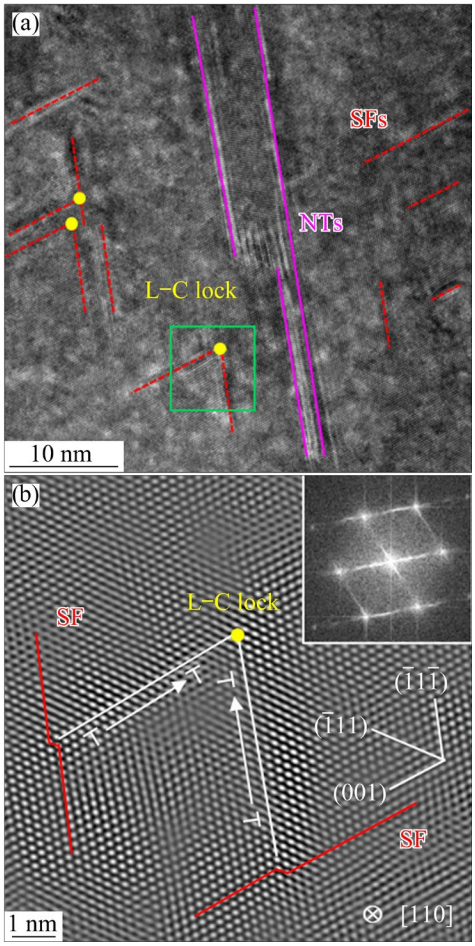

Fig. 7 (a) HRTEM image showing NTs and SFs along [110] direction; (b) IFFT atomic structure obtained from green square in (a) showing formation of L−C lock

$$a/2[110] \rightarrow a/6[12\bar{1}]+a/6[211] \quad (7a)$$

$$a/2[\bar{1}01] \rightarrow a/6[\bar{1}\,\bar{1}2]+a/6[\bar{2}11] \quad (7b)$$

$$a/6[12\bar{1}]+a/6[\bar{1}\,\bar{1}2] \rightarrow a/6[011] \quad (7c)$$

Finally, the resultant $a/6[011]$ dislocation cannot slip on the original slip planes, rendering it fixed. Actually, these immobile dislocation locks can further pin dislocations, effectively increasing the strength of the alloy [40,41]. During the deformation at 923 K, the deformation mechanism of the alloy is controlled by the SFs to shear the γ' nanoparticles, which is because the SFE decreases significantly with increasing temperature although the APB energy remains almost constant. In order to relax the stress and reduce the overall energy, the $a/2\langle 110\rangle$ dislocations with two different Burgers vectors in the $\{111\}$ plane at the γ/γ' interface interact with each other: $a/2[\bar{1}01]+a/2[0\,\bar{1}1] \rightarrow a/3[\bar{1}\,\bar{1}2]+$ SISF on (111) + $a/6[\bar{1}\,\bar{1}2]$, where the dissociated $a/3[\bar{1}\,\bar{1}2]$ dislocation cuts into the γ' phase and generates the SFs in the γ' particles [42]. By further increasing the temperature to 1023 K, the main deformation mechanism is dominated by the nanotwins to shear γ matrix and γ' particles continuously, as shown in Fig. 5. It has been demonstrated that the generation of nanotwins extending on the γ matrix and γ' nanoprecipitates during deformation is ascribed to the dissociation of $a/2[110]$ dislocations followed by the obtained $a/6\langle 112\rangle$ Shockley partial dislocations to shear the γ matrix and γ' particles, leaving behind the superlattice extrinsic stacking fault (SESF). Actually, the SESF can be considered to be the nucleation site of the nanotwins, which would be thickened by atomic rearrangement under thermal activation to form a nanotwin [43]. In addition, the L−C locks also contribute to the formation of nanotwins. It is shown that leading dislocation reacts with the sessile $a/3\langle 110\rangle$ dislocation when it moves to a L−C lock, forming two partial dislocations. These dislocations undergo double-cross slip on adjacent planes, leaving behind a Frank partial dislocation. Subsequently, the incoming Shockley dislocation effectively bypasses around the L−C lock and transforms to the upper or lower $\{111\}$ plane, which is attributed to the Burgers vector of the Frank dislocation [44]. This movement facilitates the reorganization of the crystal structure, ultimately leading to the formation of nanotwins [25,45,46]. In summary, the change in the deformation mechanism of the current superalloy leads to an increase in the elongation from 13.0% at 923 K to 17.3% at 1023 K.

5 Conclusions

(1) After solid-solution, cold-rolling and double-aging treatments, the novel Ni−Co-based wrought superalloy exhibits a special microstructure with trimodal $L1_2$-γ' nanoparticles (coarse primary γ', fine secondary γ', and tertiary γ') precipitating into the FCC-γ matrix, in which the substructures, including high-density dislocations, SFs, L−C locks, and nanotwins are introduced during the cold-rolling and remain stable even after subsequent double-aging.

(2) A higher yield strength (σ_{YS}=1855 MPa at RT, σ_{YS}=1406 MPa at 923 K, and σ_{YS}=1086 MPa at 1023 K) can be achieved in this superalloy, compared to other typical commercial wrought superalloys. The strengthening mechanisms are further discussed, indicating that the precipitation strengthening is dominant, and the high-density dislocations and nanotwins prefabricated by cold-rolling contribute to the strength increment at RT and elevated temperatures.

(3) The existence of a large number of slip bands in the aged alloy indicates that the plastic deformation during cold-rolling is controlled by the planar slip of dislocations. However, at 923 K, the deformation mechanism is dominated by SFs to shear the γ' nanoparticles, while at 1023 K, the deformation mechanism is closely related to nanotwins crossing the γ and γ' phases. This change contributes to an increase in elongation of the alloy from 13.0% at 923 K to 17.3% at 1023 K.

CRediT authorship contribution statement

Yao ZHANG: Data curation, Formal analysis, Methodology, Writing − Original draft; **Jin-lin LI:** Methodology, Visualization; **Yan-cheng LI:** Investigation, Formal analysis; **Jin-xin DONG:** Investigation, Visualization; **Cai-yu GUO:** Investigation, Supervision; **Hong-yao YU:** Supervision, Methodology, Writing − Reviewing & editing; **Qing WANG:** Conceptualization, Supervision, Writing − Reviewing & editing.

Declaration of competing interest

The authors declare that they have no known competing financial interests or personal relationships that could have appeared to influence the work reported in this paper.

Acknowledgments

This research was supported by the National Natural Science Foundation of China (No. 52171152). The authors are grateful for the technical assistance of Miss Feng-yun YU at Dalian University of Technology, China.

Supplementary Materials

Supplementary Materials in this paper can be found at: https://tnmsc.csu.edu.cn/download/10-p0818-2024-0932-Supplementary_Materials.pdf.

References

[1] REED R C. The superalloys: Fundamentals and applications [M]. Cambridge: Cambridge University Press, 2006.

[2] RAN Rong, WANG Yang, REN Fu-qiang, ZHANG Yuan-xiang, FANG Feng, ZHANG Wei-na, YUAN Guo, WANG Guo-dong. Ultra-high strength Inconel 718 alloy produced by a novel heat treatment [J]. Transactions of Nonferrous Metals Society of China, 2024, 34: 2204−2218.

[3] HUANG Xing-wei, ZHOU Xin-zhe, WANG Wei-zhen, CUI Chuan-yong, YE Heng-qiang, YANG Zhi-qing. Influence of microtwins on Portevin−Le Châtelier effect of a Ni−Co based disk superalloy [J]. Scripta Materialia, 2022, 209: 114385.

[4] LI Yan-cheng, LI Mo, WANG Qing, ZHAO Ya-jun, ZHANG Shuang, ZOU Cun-lei, LI Ying, WANG Lian-chao, DONG Chuang. Composition optimization of Inconel 718 via cluster formula and experimental verification [J]. Journal of Materials Science & Technology, 2023, 140: 249−259.

[5] SMITH T M, GOOD B S, GABB T P, ESSER B D, EGAN A J, EVANS L J, MCCOMB D W, MILLS M J. Effect of stacking fault segregation and local phase transformations on creep strength in Ni-base superalloys [J]. Acta Materialia, 2019, 172: 55−65.

[6] MONAJATI H, JAHAZI M, BAHRAMI R, YUE S. The influence of heat treatment conditions on γ' characteristics in Udimet® 720 [J]. Materials Science and Engineering A, 2004, 373: 286−293.

[7] RADIS R, SCHAFFER M, ALBU M, KOTHLEITNER G, PÖLT P, KOZESCHNIK E. Multimodal size distributions of γ' precipitates during continuous cooling of UDIMET 720 Li [J]. Acta Materialia, 2009, 57: 5739−5747.

[8] OSADA T, GU Yue-feng, NAGASHIMA N, YUAN Yong, YOKOKAWA T, HARADA H. Optimum microstructure combination for maximizing tensile strength in a poly-crystalline superalloy with a two-phase structure [J]. Acta Materialia, 2013, 61: 1820−1829.

[9] GU Yue-feng, ZHONG Zhi-hong, YUAN Yong, OSADAL T, CUI chuan-yong, YOKOKAWA T, HARADA H. An advanced cast-and-wrought superalloy (TMW-4M3) for turbine disk applications beyond 700 °C [C]//Superalloys 2012: The 12th International Symposium on Superalloys. Warrendale: TMS, 2012: 903−910.

[10] LI Xin-xu, JIA Chong-lin, ZHANG Yong, LÜ Shao-min, JIANG Zhou-hua. Cracking mechanism in as-cast GH4151 superalloy ingot with high γ' phase content [J]. Transactions of Nonferrous Metals Society of China, 2020, 30: 2697−2708.

[11] MIAO J S, SLONE C, DASARI S, GHAZISAEIDI M, BANERJEE R, GEORGE E P, MILLS M J. Ordering effects on deformation substructures and strain hardening behavior of a CrCoNi based medium entropy alloy [J]. Acta Materialia, 2021, 210: 116829.

[12] ZHU C Z, ZHANG R, CUI C Y, ZHOU Y Z, QU J L, GAN B, ZHANG B J, SUN X F. Effect of pre-strain treatment on mechanical properties of a Ni−Co base disk superalloy [J]. Journal of Alloys and Compounds, 2022, 905: 164167.

[13] SUN Hao-ran, DING Zhi-gang, SUN Hao, ZHOU Jun-jun, REN Ji-chang, HU Qing-miao, LIU Wei. An efficient scheme for accelerating the calculation of stacking fault energy in multi-principal element alloys [J]. Journal of Materials Science & Technology, 2024, 175: 204−211.

[14] YUAN Yong, GU Yue-feng, CUI Chuan-yong, OSADA T, ZHONG Zhi-hong, TETSUI T, YOKOKAWA T, HARADA H. Influence of Co content on stacking fault energy in Ni−Co base disk superalloys [J]. Journal of Materials Research, 2011, 26: 2833−2837.

[15] WANG Xing-mao, DING Yu-tian, YU Hong-yao, BI Zhong-nan, GAO Yu-bi, GAN Bin. High strength and ductility in a novel Ni-based superalloy with γ' and nanotwins/stacking faults architectures [J]. Materials Science and Engineering A, 2022, 847: 143293.

[16] YUAN Yong, GU Yue-feng, OSADA T, ZHONG Zhi-hong, YOKOKAWA T, HARADA H. Deformation mechanisms in a new disc superalloy at low and intermediate temperatures [J]. Scripta Materialia, 2012, 67: 137−140.

[17] CHEN Yue-chao, WANG Cui-ping, RUAN Jing-jing, YANG Shui-yuan, OMORI T, KAINUMA R, ISHIDA K, HAN Jia-jia, LU Yong, LIU Xing-jun. Development of low-density γ'/γ' Co−Al−Ta-based superalloys with high solvus temperature [J]. Acta Materialia, 2020, 188: 652−664.

[18] SCHNEIDER C A, RASBAND W S, ELICEIRI K W. NIH Image to ImageJ: 25 years of image analysis [J]. Nature Methods, 2012, 9: 671−675.

[19] ZHANG Yao, LI Jin-lin, LI Yan-cheng, DONG Jin-xin, GUO Cai-yu, YU Hong-yao, WANG Qing, Influence of post-processing on the microstructure and mechanical properties of high-strength Ni–Co-base wrought superalloy [J]. Intermetallics, 2024, 173: 108401.

[20] YOSHIDA T, IKEUCHI T, BHATTACHARJEE T, BAI Yu, SHIBATA A, TSUJI N. Effect of elemental combination on friction stress and Hall−Petch relationship in face-centered cubic high/medium entropy alloys [J]. Acta Materialia, 2019, 171: 201−215.

[21] TAN Li-ming, LI Yun-ping, DENG Wen-kai, LIU Yong, LIU Feng, NIE Yan, JIANG Liang. Tensile properties of three newly developed Ni-base powder metallurgy superalloys [J]. Journal of Alloys and Compounds, 2019, 804: 322−330.

[22] GU Ye-jun, STILES D, EL-AWADY J A. A statistical perspective for predicting the strength of metals: Revisiting the Hall−Petch relationship using machine learning [J]. Acta Materialia, 2024, 266: 119631.

[23] HALL E O. The deformation and ageing of mild steel: III. Discussion of results [J]. Proceedings of the Physical Society Section B, 1951, 64: 747−753.

[24] LI Fang, YUAN Ding-ling, CHEN Kang-hua, CHEN Song-yi, LI Li. A novel creep model with synergetic Orowan bypassing and climbing mechanisms in nickel-base superalloys [J]. Transactions of Nonferrous Metals Society of China, 2024, 34: 1167−1177.

[25] PANDEY P, HECZKO M, KHATAVKAR N, MAZUMDER N, SHARMA A, SINGH A, MILLS M J, CHATTOPADHYAY K. On the faulting and twinning mediated strengthening and plasticity in a γ' strengthened CoNi-based superalloy at room temperature [J]. Acta Materialia, 2023, 252: 118928.

[26] HE J Y, WANG H, HUANG H L, XU X D, CHEN M W, WU Y, LIU X J, NIEH T G, AN K, LU Z P. A precipitation-hardened high-entropy alloy with outstanding tensile properties [J]. Acta Materialia, 2016, 102: 187−196.
[27] MA Y, WANG Q, JIANG B B, LI C L, HAO J M, LI X N, DONG C, NIEH T G. Controlled formation of coherent cuboidal nanoprecipitates in body-centered cubic high-entropy alloys based on $Al_2(Ni,Co,Fe,Cr)_{14}$ compositions [J]. Acta Materialia, 2018, 147: 213−225.
[28] BOOTH-MORRISON C, DUNAND D C, SEIDMAN D N. Coarsening resistance at 400 °C of precipitation-strengthened Al−Zr−Sc−Er alloys [J]. Acta Materialia, 2011, 59: 7029−7042.
[29] HOSFORD W F. Mechanical behavior of materials [M]. 2nd ed. New York, NY: Cambridge University Press, 2005.
[30] WANG Qing, LI Zhen, PANG Shu-jie, LI Xiao-na, DONG Chuang, LIAW P K. Coherent precipitation and strengthening in compositionally complex alloys: A review [J]. Entropy, 2018, 20: 878.
[31] MELANDER A, PERSSON P A. The strength of a precipitation hardened AlZnMg alloy [J]. Acta Metallurgica, 1978, 26: 267−278.
[32] ARGON A S, POLLOCK T M. Creep resistance of CMSX-3 nickel base superalloy single crystals [J]. Acta Metallurgica et Materialia, 1992, 40: 1−30.
[33] HAZOTTE A, RACINE A, DENIS S. Internal mismatch stresses in nickel-based superalloys: A finite element approach [J]. Journal de Physique IV Proceedings, 1996, 6(C1): 119−128.
[34] ARGON A. Strengthening mechanisms in crystal plasticity [M]. Oxford: Oxford University Press, 2007.
[35] MECKING H, KOCKS U F. Kinetics of flow and strain-hardening [J]. Acta Metallurgica, 1981, 29: 1865−1875.
[36] WAN Tao, CHENG Zhao, BU Lin-feng, LU Lei. Work hardening discrepancy designing to strengthening gradient nanotwinned Cu [J]. Scripta Materialia, 2021, 201: 113975.
[37] ZHANG B B, YAN F K, ZHAO M J, TAO N R, LU K. Combined strengthening from nanotwins and nanoprecipitates in an iron-based superalloy [J]. Acta Materialia, 2018, 151: 310−320.
[38] LUO X, LI D D, YANG C, GEBERT A, LU H Z, SONG T, MA H W, KANG L M, LONG Y, LI Y Y. Circumventing the strength−ductility trade-off of β-type titanium alloys by defect engineering during laser powder bed fusion [J]. Additive Manufacturing, 2022, 51: 102640.
[39] XIAO Zhong-run, HE Jun-yang, GU Ji, GAN Bin, YU Hong-yao, BI Zhong-nan, DU Jin-hui, SONG Min. Tensile properties and deformation mechanisms of a new Ni−Co base superalloy from room temperature up to 750 °C [J]. Intermetallics, 2022, 150: 107697.
[40] CAI Y Q, TAN Y B, WANG L X, SHI W, JI X M, XIANG S. Multiple strengthening mechanisms induced by nanotwins and stacking faults in CoNiCr-superalloy MP159 [J]. Materials Science and Engineering A, 2022, 853: 143793.
[41] ZENG M T, YANG Y, TAN Y B, ZHANG W W, XIANG S, MA M, ZHAO F. Recrystallization behavior and texture evolution of cryo-rolled GH159 superalloy with an ultra-high strength [J]. Materials Characterization, 2023, 197: 112656.
[42] CHEN Q Z, KNOWLES D M. Mechanism of ⟨112⟩/3 slip initiation and anisotropy of γ' phase in CMSX-4 during creep at 750 °C and 750 MPa [J]. Materials Science and Engineering A, 2003, 356: 352−367.
[43] GODHA A, DAS D, GHOSAL P, MAKINENI S K. New insights on the interaction of solutes with the defects during creep deformation of CMSX4 Ni-based single crystal superalloy [J]. Acta Materialia, 2024, 281: 120360.
[44] QI Dong-qing, FU Bai-dong, DU Kui, YAO Ting-ting, CUI Chuan-yong, ZHANG Jian-xin, YE Heng-qiang. Temperature effects on the transition from Lomer−Cottrell locks to deformation twinning in a Ni−Co-based superalloy [J]. Scripta Materialia, 2016, 125: 24−28.
[45] LIU Nan-jun, WANG Zhang-jie, DING Jun, ASTA M, RITCHIE R O, GAN Bin, MA E, SHAN Zhi-wei. Origin of the high propensity for nanoscale deformation twins in CrCoNi medium-entropy alloy [J]. Journal of Materials Science & Technology, 2024, 183: 63−71.
[46] VORONTSOV V A, MCAULIFFE T P, HARDY M C, DYE D, BANTOUNAS, I. Precipitate dissolution during deformation induced twin thickening in a CoNi-base superalloy subject to creep [J]. Acta Materialia, 2022, 232: 117936.

固溶−轧制−时效处理 Ni−Co 基变形高温合金的力学性能和变形机理

张 垚[1]，李金临[1]，李言成[1]，董金鑫[2,3]，郭彩玉[2,4]，于鸿垚[2,4]，王 清[1]

1. 大连理工大学 材料科学与工程学院，大连 116024；
2. 钢铁研究总院 高温合金新材料北京市重点实验室，北京 100081；
3. 兰州理工大学 材料科学与工程学院，兰州 730050；
4. 北京钢研高纳科技股份有限公司，北京 100081

摘 要：为了获得高强度的 Ni−Co 基变形高温合金，在固溶和时效处理中引入冷轧工艺。使用 EBSD、SEM、TEM 和拉伸试验机对合金进行表征与测试，分析其在不同温度下的显微组织与力学性能，并揭示其强化和变形机制。结果表明，经过固溶、冷轧和双级时效处理后，合金中存在高密度位错、层错、Lomer−Cottrell 锁和纳米孪晶。合金在室温、923 和 1023 K 下的屈服强度分别为 1855、1406 和 1086 MPa，显著高于典型的镍基变形高温合金的屈服强度。这种增强主要归因于位错和纳米孪晶。此外，在冷轧过程中，塑性变形主要通过位错滑移进行。当温度升高到 923 和 1023 K 时，合金的主要变形机制分别转变为层错和纳米孪晶。

关键词：Ni−Co 基变形高温合金；力学性能；位错；层错；纳米孪晶

(Edited by Wei-ping CHEN)